Article:
Jung, H., Lee, S., Jin, X. et al. (2024) Low excess noise and high quantum efficiency avalanche photodiodes for beyond 2 μm wavelength detection. Communications Materials, 5 (1). 219. ISSN: 2662-4443

https://doi.org/10.1038/s43246-024-00627-9

communications materials

Article

https://doi.org/10.1038/s43246-024-00627-9

Low excess noise and high quantum efficiency avalanche photodiodes for beyond 2 μm wavelength detection

Check for updates

Hyemin Jung [1,2,5], Seunghyun Lee [1,2,5], Xiao Jin[3,5], Yifan Liu [3], Theodore. J. Ronningen [1], Christopher. H. Grein[4], John. P. R. David [3] & Sanjay Krishna [1]

The rising concentration of greenhouse gases, especially methane and carbon dioxide, is driving global temperature increases and exacerbating the climate crisis. Monitoring these gases requires detectors that operate in the extended short-wavelength infrared range (~2.4 μm), covering methane (1.65 μm) and carbon dioxide (2.05 μm) wavelengths. Here, we present a high-performance linear mode avalanche photodetector (APD) with an InGaAs/GaAsSb type-II superlattice absorber and an AlGaAsSb multiplier, matched to InP substrates. This APD achieves a room temperature gain of 178, an external quantum efficiency of 3560% at 2 μm, low excess noise (less than 2 at gains below 20), and a small temperature coefficient of breakdown (7.58 mV/K·μm). These results indicate that a manufacturable semiconductor material-based APD could significantly advance high-sensitivity receivers for greenhouse gas monitoring, potentially enabling their commercial production and widespread use.

The concentration of greenhouse gases such as CH_4 and CO_2 has continuously risen in the last few decades, resulting in increased global temperatures, and raising concerns about a global climate crisis. Integrated path differential absorption (IPDA) and differential absorption LIDAR (DIAL) methods have been used as standard techniques for the measurement of trace atmospheric constituents. These methods are widely used in both ground-based[1,2] and airborne[3] research, establishing a foundation for potential future spaceborne missions[4]. To monitor greenhouse gas concentrations, it is, therefore, essential to have a detector that covers the extended short-wavelength infrared (eSWIR, ~ 2.6 μm) range since CH_4 (1.65 μm)[5] and CO_2 (2.05 μm)[6–8] have absorption features associated with vibration of the C-H and C-C stretch in this wavelength range. However, conventional *p-i-n* detectors are not suitable due to the reduction in signals received over long distances and harsh environments. Instead, avalanche photodiodes (APDs) are an attractive option because of the higher sensitivity provided by their internal multiplication gain, *M*. However, APDs have a stochastic gain mechanism that gives rise to excess noise simultaneously with signal multiplication, which poses a challenge in improving the signal-to-noise ratio. McIntyre's local field theory quantifies the excess noise factor, $F(M)$, as $F(M) = kM + (1\text{-}k)(2 - 1/M)$, where k is the ratio of impact ionization coefficients (β/α for electron APDs and α/β for hole APDs)[9]. Thus, the selection of a material with a small impact ionization coefficient ratio is crucial to reduce $F(M)$.

Currently, HgCdTe (MCT) is the material of choice for high performance eSWIR and mid-wave infrared (MWIR) APDs because it provides high $M \sim 6100$ and extremely low $F(M) \sim 1.3$[10]. However, its high dark current from the narrow band gap necessitates a cooling system for efficient operation (at 77–110 K)[10]. Additionally, producing MCT with high uniformity is challenging, and the manufacturing process has low yield leading to increased cost. As such, researchers are seeking alternative materials. InAs is an emerging technology for SWIR APDs that offers a low $F(M) \sim 1.6$[11]. However, the narrow bandgap of the InAs also leads to a high tunneling dark current and the Fermi-level pinning in InAs increases the surface leakage current making it challenging to operate at temperatures above 77 K[11].

In general, for the eSWIR range, traditional *p-i-n* structure APDs are subject to the dominance of dark currents from the band-to-band tunneling mechanism, resulting from the narrow energy bandgap and high electric field, thereby making signal amplification difficult. To address this challenge, a separate absorption, charge, and multiplication (SACM) structure can be used to spatially isolate the absorption and multiplication regions. The SACM structure effectively suppresses the band-to-band tunneling mechanism, thereby enhancing the APD's ability to maintain a high electric field only in the wider gap multiplication region while keeping the electric

[1]Department of Electrical and Computer Engineering, The Ohio State University, Columbus, Ohio, 43210, USA. [2]Department of Electrical Engineering, University of Texas at Arlington, Arlington, Texas, 76019, USA. [3]Department of Electronic and Electrical Engineering, University of Sheffield, Sheffield, S1 3JD, UK. [4]Department of Physics, University of Illinois, Chicago, Illinois, 60607, USA. [5]These authors contributed equally: Hyemin Jung, Seunghyun Lee, Xiao Jin. e-mail: krishna.53@osu.edu

field in the narrower gap absorber lower than its tunneling threshold. As a result, the SACM structure offers a significant advantage by reducing tunneling-induced noise while maintaining a high gain.

In 2020, Jones et al. demonstrated an $Al_xIn_{1-x}As_ySb_{1-y}$ (AlInAsSb)-based SACM APD on a GaSb substrate, detecting 2 µm wavelength[12]. This SACM APD presented a low excess noise (corresponding to $k \sim 0.01$) and low dark current density ($J_d \sim 33$ mA/cm at $M = 10$) with an external quantum efficiency (EQE) of 20 % at 2 µm (at a punch-through, V_{PT}). Although the results are encouraging, the use of expensive GaSb substrates and more importantly, the complicated digital growth technique may hamper widespread adoption. To circumvent these limitations, we have been exploring an antimonide based SACM structure lattice matched to an InP substrate which is a commercial platform because of their affordability in a large area and low cost. There is a well-developed InGaAs/GaAsSb type-II superlattice (T2SL) absorber on InP[13,14], whose absorption spectrum can be extended to the eSWIR range. This absorber also can readily be grown because of the relatively thick layers of each T2SL constituent (5 nm) with each layer being lattice matched to InP. In 2006, Sidhu et al.[15] reported a SACM APD with a 5 nm-InGaAs/5 nm-GaAsSb T2SL absorber with an InP multiplier. The device provided $M > 30$ at room temperature and a cut-off wavelength of 2.4 µm. However, its performance was limited by the high excess noise of the InP ($k \sim 0.5$) multiplication region. A few years later, Goh et al.[16] and Ong et al.[17] demonstrated APDs with InGaAs/GaAsSb T2SL absorbers with a slightly lower excess noise InAlAs multiplier. These devices demonstrated EQE of about 20% at 2 µm operating at room temperature. Although the excess noise was reduced by replacing InP with InAlAs ($k \sim 0.2$), it still requires improvement to meet the demands of the current application and to be comparable to the performance of the AlInAsSb SACM APDs on GaSb substrates.

$Al_xGa_{1-x}As_ySb_{1-y}$ is a quaternary alloy that can be grown lattice-matched on InP. Initial work by Yi et al.[18,19] showed that $AlAs_{0.56}Sb_{0.44}$ (AlAsSb) can give rise to a very large α/β ratio in thick bulk structures and a very low $F(M)$ of ~2.1 and $M \sim 36$. More recently, Lee et al.[20] have explored $Al_{0.85}Ga_{0.15}AsSb$ (AlGaAsSb) with a 1000 nm-thick unintentionally doped layer grown as a random alloy, lattice-matched to the InP substrate. Their findings revealed that this material has a remarkably low excess noise corresponding to $k \sim 0.01$, with a gain of up to 278 achievable under 1550 nm illumination while operating at room temperature. Consequently, it has emerged as a promising material candidate for next-generation APD technology. In this paper, we have combined the AlGaAsSb multiplier with an InGaAs/GaAsSb T2SL absorber, both lattice-matched to an InP substrate, to achieve high-performance SACM APDs for eSWIR detection (cutoff ~2.4 µm). Our device exhibits high gain-quantum efficiency product (3560 % at 2 µm), low excess noise ($F < 2$ at $M < 20$), and high gain ($M \sim 178$) at room temperature, providing advanced eSWIR SACM APD performance on an InP substrate. These results demonstrate the potential of this material combination for use in eSWIR detection.

Results

Device design and simulation

The high-performance SACM APDs designed for eSWIR detection require high material quality with low impurity concentrations. The unintentionally doped (UID) layer thicknesses for the absorber and the multiplier were designed to be 1500 nm and 1000 nm, respectively, with the specific structural details as illustrated in Fig. 1a. The $Al_xGa_{1-x}As_ySb_{1-y}$ grading layer between the absorber and the multiplier is composed of three different Al compositions: 0, 25, and 55%. The AlGaAsSb quaternary material in this SACM APD was grown as a random alloy, and it utilized a InGaAs/GaAsSb T2SL absorber lattice matched to the InP substrate, both of which can be provided by a commercial foundry. Details of the material growth and X-ray diffraction (XRD) results of this device are provided in the *Methods* and the Supplementary Information (S1), respectively. The simulated electric fields and energy band profiles of the device at zero, V_{PT}, and operational (V_{OP}) bias after punch-through are illustrated in Fig. 1b, c, respectively, and were obtained using Silvaco software. Here, V_{OP} is −87 V, where avalanche multiplication occurs. A well-designed grading layer between the absorber and multiplier allows for smooth electron transport over the operational bias range.

Capacitance-voltage, current-voltage, and gain

Capacitance-voltage (C-V) measurements were carried out to identify the doping profile and the depletion width of an InGaAs/GaAsSb T2SL-based SACM APD, as shown in Fig. 2a. A sudden drop in capacitance around −48 V indicates the occurrence of punch-through. The simulated C-V curve by a 1D Poisson solver closely matches the measured V_{PT}, as indicated by the dotted black line. The inset in Fig. 2a shows that the Be dopants appear to have undergone some diffusion, resulting in a secondary peak at the start of the T2SL region. The integrated charge is only 2.8% higher than the design value. The total thickness of the InGaAs/GaAsSb T2SL absorber was modeled as 1400 nm, similar to values obtained from XRD (see *S1* in *Supplementary Information*). Both the absorber and multiplier have background doping concentrations of 1×10^{15} and 4×10^{15} cm^{-3}, respectively. Figure 2b shows the dark current density of devices with 150, 200, 250, and 300 µm diameters. The dark current densities increase sharply at −48 V,

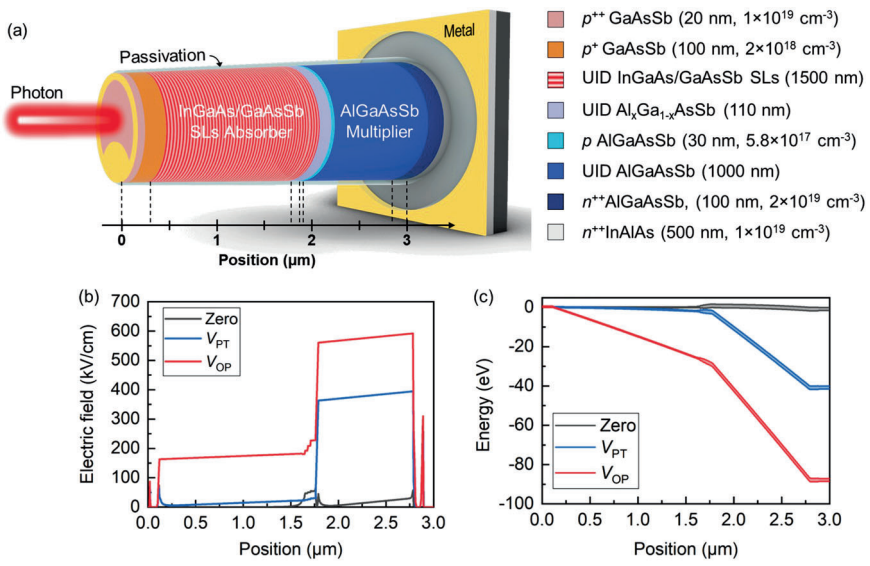

Fig. 1 | Design and simulation of the eSWIR SACM APD. a Schematic eSWIR SACM APD device structure with InGaAs/GaAsSb T2SL absorber and AlGaAsSb multiplier. **b** Simulated electric fields, and (**c**) band profiles of the eSWIR SACM APD with a nominal thickness at zero, punch-through (V_{PT}), and operating (V_{OP}) bias.

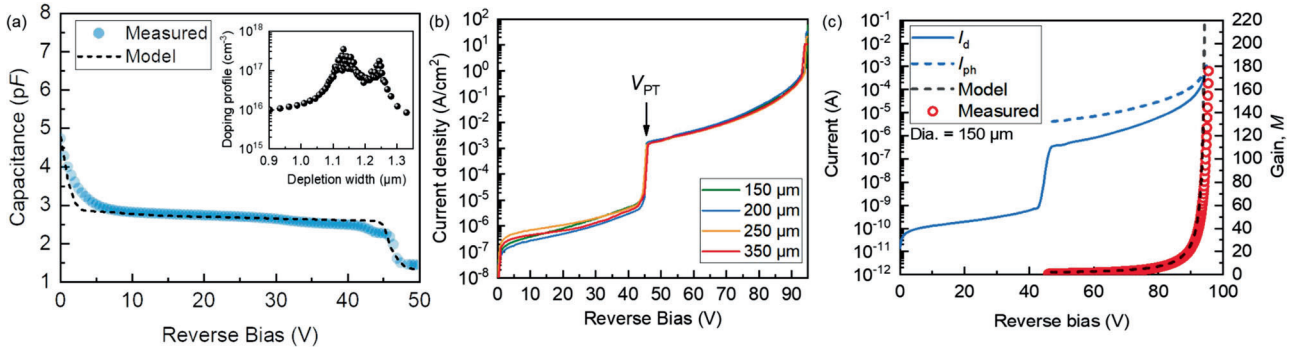

Fig. 2 | Electrical and optical characterizations of the eSWIR SACM APD. **a** Measured (blue dot) and simulated (black-dashed line) capacitance-voltage results. Inset in (**a**) shows the doping profile of the charge sheet layer. **b** Dark current density from various sized devices as a function of reverse bias. The punch-through (V_{PT}) happens at around 48 V in both *C-V* and *I-V*. **c** Shows photocurrent and gain from 150 μm device obtained with 940 nm illumination. The measured gain agrees well with the fitted curve modeled using impact ionization coefficients of the AlGaAsSb.

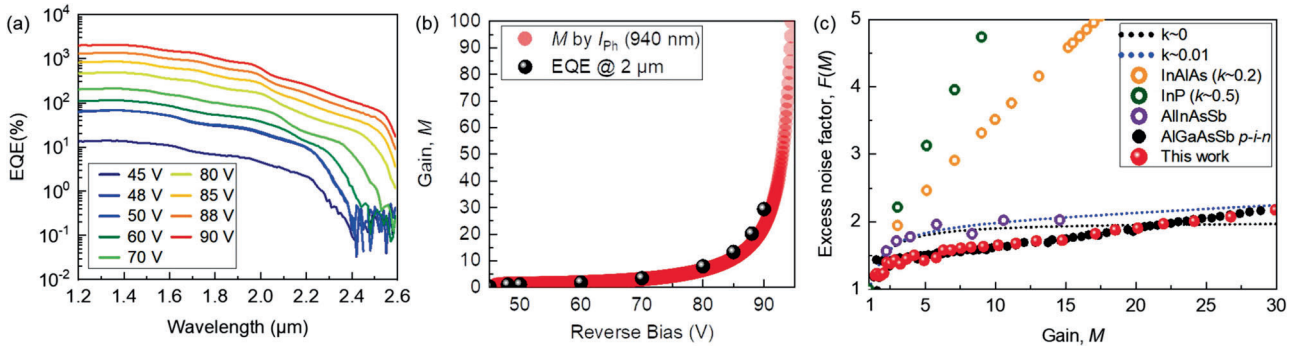

Fig. 3 | Detector characterization of the eSWIR SACM APD. **a** EQE of eSWIR SACM APD at various applied biases, and (**b**) extracted gain from EQE at 2 μm compared to the gain obtained by photocurrent under 940 nm laser illumination as a function of reverse bias. **c** Measured excess noise as a function of gain with other emerging III-V-based SACM APDs[12,15,17] and theoretical values based on the McIntyre local field model when $k \sim 0$ (black-dashed line) and $k \sim 0.01$ (blue-dashed line).

consistent with the V_{PT} obtained from the *C-V* curve. The dark current densities do not scale with the area before punch-through, however are overlapped after punch-through, suggesting that the dark currents of the multiplier and absorber were limited by the surface component and the bulk component, respectively. The gain curve in Fig. 2c was obtained under 940 nm wavelength illumination at room temperature, and the dotted black line is a fitted curve simulated by using the Random Path Length (RPL) model[21] with $M = 1$ at 48 V. Details on the determination of the unity gain point can be found in the methods section. The maximum gain our SACM APD achieved was about 178, but this value was limited by edge breakdown rather than the inherent characteristics of the devices. A well-designed planar device architecture should provide a much higher gain value.

External quantum efficiency and excess noise

Spectral response measurements were used to determine the EQE of the extended SACM APDs. Figure 3a displays the spectral EQE obtained from the relative responsivities of a SACM APD under various voltages at room temperature. The device has a cutoff wavelength of ~2.4 μm, and the EQE at 2 μm was 20 % at −48 V and remained constant until −50 V, indicating that the punch-through at −48 V is consistent with the values obtained from *C-V* and *I-V*. The device can achieve a gain×QE product up to 3560% at 2 μm, and the multiplication calculated from the EQE results at 2 μm compares very well with the gain obtained by the photocurrent, as shown in Fig. 3b.

Figure 3c shows the measured $F(M)$ of this SACM APD using the setup as detailed in the Methods section. Notably, our device exhibits an exceptionally low $F(M)$, nearing $F(M) \sim 1.7$ at $M = 10$. This SACM APD excess noise result is almost identical to that of a similar composition and multiplication region thickness AlGaAsSb *p-i-n* reported previously[22]. This value is approximately two times lower than that achieved in previous research involving the InGaAs/GaAsSb T2SL with an InAlAs multiplier on InP[17]. Furthermore, our T2SL SACM APD can have a 2.5 times higher operating gain value ($M = 25$) for the equivalent $F(M = 10)$ of AlInAsSb APDs grown on InP. For M less than 20, the only APD that has exhibited noise performance superior to our device is a MCT APD[10,23]. However, it is crucial to note that the MCT requires operation at considerably lower temperatures, typically within the range of 77 to 110 K[10,23,24], thereby presenting challenges in terms of high cost, size, weight, and power (c-SWaP). Additionally, the $F(M)$ of this work is even lower than McIntyre's local field model limit at $M < 20$, possibly due to the non-exponential Weibull-Fréchet probability distribution function of the impact ionization process[22].

Temperature coefficient of breakdown

One of the essential performance metrics in APDs is the temperature coefficient of breakdown (C_{bd}), which is defined as the rate of change in the breakdown voltage with temperature. Normally, the breakdown voltage of an APD tends to increase as the temperature rises, primarily due to enhanced phonon scattering reducing the ionization coefficients. This phenomenon can have a significant impact on the gain, and consequently, the sensitivity of APDs made from materials such as InP and Si, where C_{bd} is large.

Any change in breakdown voltage necessitates the incorporation of temperature stabilization in a LiDAR system. Therefore, it is advantageous to have a low C_{bd}, especially since bulky temperature control systems are not

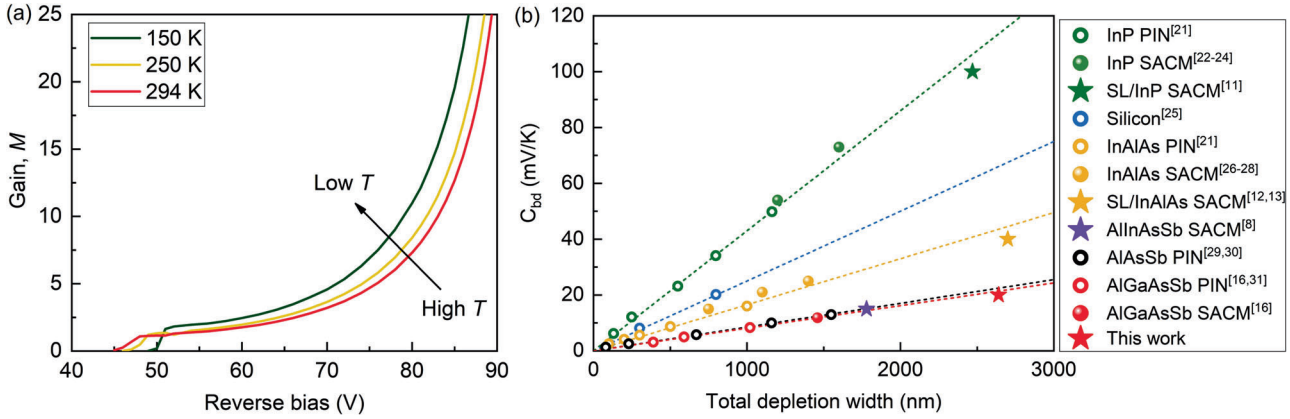

Fig. 4 | Temperature stability of breakdown voltage in the eSWIR SACM APD. a Measured gain, *M*, as a function of reverse bias at three different temperatures: 150, 250, and 294 K. **b** C_{bd} versus total depletion width for APDs of various materials: InP[15,25–28], Si[29], InAlAs[16,17,25,30–32], AlInAsSb[12], AlAsSb[33,34], and AlGaAsSb[20,35]. Star symbol refers to devices operating at ≥ 2 μm wavelength.

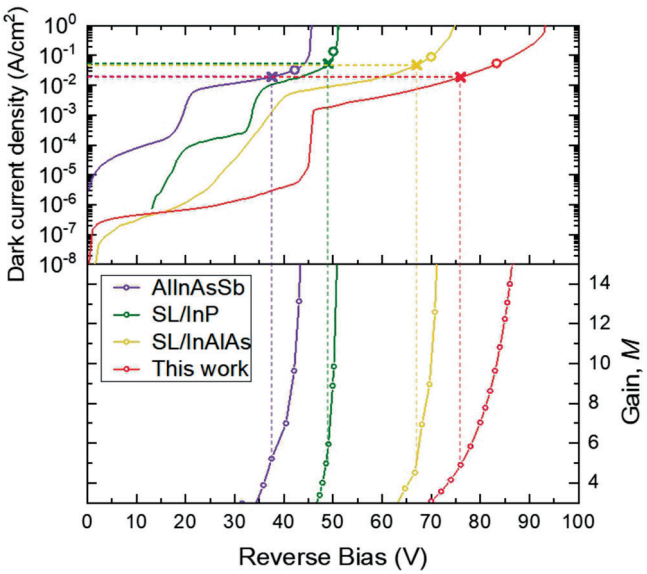

Fig. 5 | Dark-current comparison of this work with other emerging III-V eSWIR SACM APDs. Dark current density (upper) and gain (lower) vs. reverse bias of this work (red) compared with other emerging III-V eSWIR SACM APDs: AlInAsSb (purple)[12], InGaAs/GaAsSb T2SL with InP (green)[15] and InGaAs/GaAsSb with InAlAs (yellow)[16]. The cross and circular marks on each dark current density curve indicate the dark current density where $M = 5$ and $M = 10$, respectively.

favored in spaceborne or airborne lidar systems, which aim to minimize their size, weight, and power consumption.

To attain the C_{bd} of our device, gain measurements were conducted at different temperatures: 150, 250, and 294 K, as depicted in Fig. 4. The assessment of the voltage change with temperature was performed at $M = 25$ rather than at the actual breakdown point. This approach was chosen to yield similar results while minimizing the risk of catastrophic damage to the devices. The accurate determination of the device junction temperatures was carried out using the methodology outlined elsewhere[34]. The measured C_{bd} is approximately 20 mV/K for the total thickness of 2640 nm, which is approximately 4.75 and 2 times lower than the value observed for the 2470 nm thick T2SL/InP SACM APD (100 mV/K)[15], the 2755 nm T2SL/InAlAs SACM APD (~ 40 mV/K)[16,17], respectively, and was similar to a 1780 nm thick AlInAsSb SACM APD (~ 18 mV/K)[12]. However, it should be noted that C_{bd} is a function of the total device width (see Fig. 4b). When we normalize our C_{bd} by the total thickness in μm (C_{bd} /μm), it is apparent that our SACM APD has a C_{bd} /μm of 7.58 mV/K·μm which is smaller than 8.43 mV/K·μm for AlInAsSb SACM APD. The C_{bd} of our SACM APD is, therefore, extremely low compared to other T2SL SACMs, even though their total thicknesses are similar.

Discussion

The dark current density of our T2SL SACM APD is compared with other emerging III-V eSWIR SACM APDs in Fig. 5. In particular, the dark current density after V_{pt} is of interest since shot noise of a SACM APD is proportional to the square root of the dark current at the operating bias. After V_{pt}, our device shows the dark current density that is one order of magnitude lower than other APDs. As the applied reverse voltage increases, the dark current density of our device rapidly increases and finally becomes comparable to others. However, it is important to highlight that this elevated dark current density can be effectively reduced through careful device design optimization, for example, by increasing the charge sheet doping or thickness so that the electric field in the T2SL absorber is reduced while the field in the multiplication region increases This design would not only reduce the dark current in the absorber while enhancing the gain, but would also reduce the operating bias as well.

Table 1 presents a comparative analysis of our work alongside other emerging III-V-based eSWIR APDs, including an AlInAsSb SACM APD on GaSb, and an InGaAs/GaAsSb T2SL SACM APD with InP and InAlAs multipliers. Our AlGaAsSb-based SACM APD, incorporating an InGaAs/GaAsSb T2SL, stands out for its exceptional performance in all metrics. Especially, it achieves the lowest $F(M)$ at $M \sim 10$ and exhibits the lowest dark current density at V_{PT} and even at $M \sim 5$. While our SACM APD shows a slightly higher dark current density at $M \sim 10$ (55 A/cm^2) when compared to the AlInAsSb SACM APD device B (33 mA/cm^2) it should be noted that our device features a cut-off at 2.4 μm (0.516 eV), in contrast to the 2.1 μm (0.59 eV) cut-off of AlInAsSb, which constitutes a significant energy difference of 0.074 eV. To compare these two materials more fairly, one should refer to the IGA-17 Rule as depicted in the *Supplementary Information (see* Fig. S2*)*, which shows that the dark current of the results shown here relative to the bandgap is actually very low. Temperature dependence of the dark currents from 300 K to 240 K showed an activation energy of 0.375 meV (see Figs. S3, S4 in Supplementary Information) in good agreement with the activation energies reported for other T2SL structures[15]. The longer cutoff wavelength of 2.4 μm in our structure c.f. the AlInAsSb APD means that more cooling can be applied to reduce the dark currents without losing the ability to operate at 2 μm.

Conclusions

In this work, we have demonstrated SACM APDs with antimonide-based materials on InP substrates for efficient detection beyond 2 μm wavelength at room temperature. At 2 μm wavelength, our device exhibits a multiplied

Table 1 | Comparison of this work with other emerging III-V eSWIR SACM APDs[12,15,16]

Materials	AlInAsSb (Device B)	InGaAsSb SL/ InP	InGaAsSb SL/InAlAs	This work
Substrate	GaSb	InP	InP	InP
Max reported M	150	35	60	180
J_d @ V_{PT}	8 mA/cm^2	8.55 mA/cm^2 (M~1.7)	5 mA/cm^2	1.9 mA/cm^2
J_d @ M = 5	19 mA/cm^2	54 mA/cm^2	48 mA/cm^2	18 mA/cm^2
J_d @ M = 10	33 mA/cm^2	136 mA/cm^2	90 mA/cm^2	55 mA/cm^2
$F(M = 10)$	2.02	5.13	3.51	1.65
Cut-off λ	2.1 μm	2.4 μm	2.5 μm	2.4 μm
C_{bd}/W	8.43 mV/K·μm	40.49 mV/K·μm	14.52 mV/K·μm	7.58 mV/K·μm

QE of 3560 % (M = 178) with extremely low excess noise (F < 2 at M < 20) at room temperature and a smallest temperature coefficient of breakdown (C_{bd}/μm = 7.58 mV/K·μm) among other III-V APD technologies on InP substrate. In addition to being grown on a standard InP substrate, the multiplication region and the T2SL absorber regions are grown using well-established growth techniques, meaning that these APDs can be easily manufactured.

Methods

Material growth

The eSWIR SACM APD was grown on n-InP substrates using a solid-state MBE reactor. For group V cells, we used RIBER VAC 500 and Veeco Mark V valved crackers for As and Sb, respectively. To achieve very low background doping concentration for both InGaAs/GaAsSb SL and random alloy AlGaAsSb, the calibration growths and several p^+-i-n^+ growths were performed at various growth conditions such as growth rate, V/III beam equivalent pressure (BEP) ratio, and growth temperature. More details on the growth can be found elsewhere[36–38].

Device fabrication

To assess the performance of the device, the epi materials underwent fabrication using citric-based wet chemicals for mesa delineation. Subsequently, the device's sidewall was covered by SU8 to suppress the surface leakage current. Finally, Ti/Au (12/150 nm) was deposited for top and bottom n-contacts using an e-beam evaporator.

I-V and C-V measurements

The electrical performances of the device were assessed by I-V and C-V characteristics. The I-V characteristics were measured using a probe station and an HP4140B picoammeter. C-V measurements were undertaken using an HP4275A LCR meter as a frequency of 10 KHz. To calculate the depletion width and background doping concentration of the device, a static dielectric constant of 11.4 was used for the AlGaAsSb multiplier, and a value of ~14 was taken as an average weight for InGaAs and GaAsSb.

Unity gain determination

The M = 1 was assumed to be at a reverse bias of 48 V. This was determined by obtaining the electric field profile of the structure from capacitance voltage measurements and then calculating the multiplication as a function of reverse bias using published ionization coefficient data. The calculated M fits the experimental measurements very closely. The excess noise, F, in the SACM APD was compared to that of a similar composition and thickness AlGaAsSb p-i-n diode from the literature. An assumption of M = 1 at 48 V gave identical F to that obtained from the p-i-n diode suggesting that the unity gain point was correctly determined.

Multiplication and excess noise

A transimpedance-amplifier-based circuit is employed to assess the multiplication and excess noise in these structures, featuring a center frequency of 10 MHz and bandwidth of 4.2 MHz as described in elsewhere[39]. To eliminate the effects of the DC leakage current, we utilized phase-sensitive detection. The shot noise was calibrated by using a reference device (SFH2701 Silicon PIN photodiode). To determine the excess noise factor of the AlGaAsSb-based eSWIR APD, the measured noise power of our device was compared to the measured noise power of the reference device at a given photocurrent. A Thorlabs fiber-coupled LED (M1450F1) was used to illuminate 1450 nm on the devices to measure the multiplication and the excess noise. The unity gain value of the T2SL/AlGaAsSb SACM was determined by fitting the multiplication curve to the random path length model.

Quantum efficiency

QE measurements involved illuminating a 100 W tungsten bulb into a monochromator (IHR320), which was focused onto the device under test using optical lenses, while the photocurrent was measured using a lock-in amplifier. A mechanical chopper modulated the light at 180 Hz to remove DC dark current, and a Keithley 236 source meter unit was used to apply the bias. As a reference sample, a commercial extended InGaAs photodiode (Thorlabs FD05D) was used to determine the relative power of the monochromator at each wavelength with known responsivity.

Data availability

The data that support the plots within this paper and other finding of this study are available from the corresponding authors upon reasonable request.

Received: 15 July 2024; Accepted: 29 August 2024;
Published online: 09 October 2024

References

1. Abshire, J. B. et al. Airborne measurements of CO_2 column absorption and range using a pulsed direct-detection integrated path differential absorption lidar. *Appl. Opt.* **52**, 4446–4461 (2013).
2. Wagner, G. A. & Plusquellic, D. F. Ground-based, integrated path differential absorption LIDAR measurement of CO_2, CH_4, and H_2O near 1.6 μm. *Appl. Opt.* **55**, 6292–6310 (2016).

3. Wirth, M. et al. The airborne multi-wavelength water vapor differential absorption lidar WALES: system design and performance. *Appl. Phys. B* **96**, 201–213 (2009).
4. Ehret, G. et al. MERLIN: A French-German space lidar mission dedicated to atmospheric methane. *Remote Sens.* **9**, 1052 (2017).
5. Barton-Grimley, R. A. et al. Evaluation of the High Altitude Lidar Observatory (HALO) methane retrievals during the summer 2019 ACT-America campaign. *Atmos. Meas. Tech.* **15**, 4623–4650 (2022).
6. Singh, U. N. et al. Feasibility study of a space-based high pulse energy 2 µm CO 2 IPDA lidar. *Appl. Opt.* **56**, 6531–6547 (2017).
7. Refaat, T. F. et al. Airborne Testing of 2-µm Pulsed IPDA Lidar for Active Remote Sensing of Atmospheric Carbon Dioxide. *Atmosphere* **12**, 412 (2021).
8. Refaat, T. F., Petros, M., Singh, U. N., Antill, C. W. & Remus, R. G. High-Precision and High-Accuracy Column Dry-Air Mixing Ratio Measurement of Carbon Dioxide Using Pulsed 2-$\mu $ m IPDA Lidar.*IEEE Transactions on Geoscience and Remote Sensing* **58**, 5804–5819 (2020).
9. McIntyre, R. Multiplication noise in uniform avalanche diodes. *IEEE Trans. Electron Devices* **13**, 164–168 (1966).
10. Anderson, P. D. et al. Recent advancements in HgCdTe APDs for space applications. *J. Electron. Mater.* **51**, 6803–6814 (2022).
11. Ker, P. J., David, J. P. & Tan, C. H. Temperature dependence of gain and excess noise in InAs electron avalanche photodiodes. *Opt. express* **20**, 29568–29576 (2012).
12. Jones, A. H., March, S. D., Bank, S. R. & Campbell, J. C. Low-noise high-temperature AlInAsSb/GaSb avalanche photodiodes for 2 µm applications. *Nat. Photonics* **14**, 559–563 (2020).
13. Uliel, Y. et al. InGaAs/GaAsSb Type-II superlattice based photodiodes for short wave infrared detection. *Infrared Phys. Technol.* **84**, 63–71 (2017).
14. Sidhu, R., Duan, N., Campbell, J. C. & Holmes, A. L. A long-wavelength photodiode on InP using lattice-matched GaInAs-GaAsSb type-II quantum wells. *IEEE photonics Technol. Lett.* **17**, 2715–2717 (2005).
15. Sidhu, R. et al. 2.4 µm cutoff wavelength avalanche photodiode on InP substrate. *Electron. Lett.* **42**, 181–182 (2006).
16. Goh, Y. L. et al. in *Infrared Technology and Applications XXXV*. 1204–1213 (SPIE).
17. Ong, D. S. et al. InAlAs Avalanche Photodiode With Type-II Superlattice Absorber for Detection Beyond 2$\mu\hbox {m} $. *IEEE Transactions on Electron Devices* **58**, 486–489 (2010).
18. Yi, X. et al. Demonstration of large ionization coefficient ratio in AlAs 0.56 Sb 0.44 lattice matched to InP. *Sci. Rep.* **8**, 9107 (2018).
19. Yi, X. et al. Extremely low excess noise and high sensitivity AlAs 0.56 Sb 0.44 avalanche photodiodes. *Nat. Photonics* **13**, 683–686 (2019).
20. Lee, S. et al. High gain, low noise 1550 nm GaAsSb/AlGaAsSb avalanche photodiodes. *Optica* **10**, 147–154 (2023).
21. Ong, D., Li, K., Rees, G., David, J. & Robson, P. A simple model to determine multiplication and noise in avalanche photodiodes. *J. Appl. Phys.* **83**, 3426–3428 (1998).
22. Finger, G. et al. Scientific detector workshop 2022 on-sky performance verification of near-infrared e− APD technology for wavefront sensing and demonstration of e− APD pixel performance to improve the sensitivity of large science focal planes. *Astron. Nachr.*, **344**, e20230069 (2023).
23. Sun, X. et al. HgCdTe avalanche photodiode detectors for airborne and spaceborne lidar at infrared wavelengths. *Opt. express* **25**, 16589–16602 (2017).
24. Lewis, H. I. et al. Anomalous excess noise behavior in thick Al0. 85Ga0. 15As0. 56Sb0. 44 avalanche photodiodes. *Sci. Rep.* **13**, 9936 (2023).
25. Tan, L. J. J. et al. Temperature dependence of avalanche breakdown in InP and InAlAs. *IEEE J. Quantum Electron.* **46**, 1153–1157 (2010).
26. Hyun, K.-S. & Park, C.-Y. Breakdown characteristics in InP/InGaAs avalanche photodiode with pin multiplication layer structure. *J. Appl. Phys.* **81**, 974–984 (1997).
27. Tarof, L., Yu, J., Baird, T., Bruce, R. & Knight, D. Temperature measurements of separate absorption, grading, charge, and multiplication (SAGCM) InP/InGaAs avalanche photodiodes (APD's). *IEEE photonics Technol. Lett.* **5**, 1044–1046 (1993).
28. Ma, C. F., Deen, M. J., Tarof, L. E. & Yu, J. C. Temperature dependence of breakdown voltages in separate absorption, grading, charge, and multiplication InP/InGaAs avalanche photodiodes. *IEEE Trans. Electron Devices* **42**, 810–818 (1995).
29. Massey, D., David, J. & Rees, G. Temperature dependence of impact ionization in submicrometer silicon devices. *IEEE Trans. Electron Devices* **53**, 2328–2334 (2006).
30. Levine, B. et al. A new planar InGaAs–InAlAs avalanche photodiode. *IEEE photonics Technol. Lett.* **18**, 1898–1900 (2006).
31. Rouvie, A. et al. High Gain $\times $ Bandwidth Product Over 140-GHz Planar Junction AlInAs Avalanche Photodiodes. *IEEE Photonics Technol. Lett.* **20**, 455–457 (2008).
32. Ishimura, E. et al. Degradation mode analysis on highly reliable guardring-free planar InAlAs avalanche photodiodes. *J. Lightwave Technol.* **25**, 3686–3693 (2007).
33. Xie, S. & Tan, C. H. AlAsSb avalanche photodiodes with a sub-mV/K temperature coefficient of breakdown voltage. *IEEE J. Quantum Electron.* **47**, 1391–1395 (2011).
34. Jin, X. et al. Temperature dependence of the impact ionization coefficients in AlAsSb lattice matched to InP. *IEEE J. Sel. Top. Quantum Electron.* **28**, 1–8 (2021).
35. Guo, B. et al. Temperature dependence of avalanche breakdown of AlGaAsSb and AlInAsSb avalanche photodiodes. *J. Lightwave Technol.* **40**, 5934–5942 (2022).
36. Jung, H. et al. in *Infrared Technology and Applications XLVIII*. 96–104 (SPIE).
37. Lee, S. et al. Random alloy thick AlGaAsSb avalanche photodiodes on InP substrates. *Appl. Phys. Lett.* **120**, 071101 (2022).
38. Jung, H. et al. High electric field characteristics of GaAsSb photodiodes on InP substrates. *Appl. Phys. Lett.* **122**, 221102-1–221102-6 (2023).
39. Lau, K. et al. Excess noise measurement in avalanche photodiodes using a transimpedance amplifier front-end. *Meas. Sci. Technol.* **17**, 1941 (2006).

Acknowledgements

This work was supported by the Advanced Component Technology (ACT) Program of NASA's Earth Science Technology Office (ESTO) under Grant No. 80NSSC21K0613.

Author contributions

H.J. and S.L. designed the structures and performed material growth, fabrication, and preliminary device characterizations for all InGaAs/GaAsSb superlattice/AlGaAsSb SACM structures. X.J. and Y.L. undertook IV, CV, QE, multiplication, and excess noise for the SACM structure. All authors discussed and analyzed the results, and H. J., S.L., X.J., Y.L., T.J.R., C.H.G., J.P.R.D., and S.K. wrote the manuscript. J.P.R.D. helped with data analysis and S.K. supervised the entire project. All authors reviewed and approved the manuscript.

Competing interests

The authors declare no competing interests.

Additional information

Supplementary information The online version contains supplementary material available at https://doi.org/10.1038/s43246-024-00627-9.

Correspondence and requests for materials should be addressed to Sanjay Krishna.

Peer review information *Communications Materials* thanks the anonymous reviewers for their contribution to the peer review of this work. Primary Handling Editors: John Plummer.